



# The impact of surface composition on the interfacial energetics and photoelectrochemical properties of BiVO<sub>4</sub>

Dongho Lee<sup>1,7</sup>, Wennie Wang<sup>2,7</sup>, Chenyu Zhou<sup>3,4,7</sup>, Xiao Tong<sup>3</sup>, Mingzhao Liu<sup>3</sup>✉, Giulia Galli<sup>2,5,6</sup>✉ and Kyoung-Shin Choi<sup>1</sup>✉

**The ability to engineer a photoelectrode surface is pivotal for optimizing the properties of any photoelectrode used for solar fuel production. Altering crystal facets exposed on the surface of photoelectrodes has been a major strategy to modify their surface structure. However, there exist numerous ways to terminate the surface even for the same facet, which can considerably alter the photoelectrode properties. Here we report tightly integrated experimental and computational investigations of epitaxial BiVO<sub>4</sub> photoelectrodes with vanadium- and bismuth-rich (010) facets. Our study demonstrates that even for the same facet the surface Bi:V ratio has a remarkable impact on the interfacial energetics and photoelectrochemical properties. We also elucidate the microscopic origins of how the surface composition can affect the photoelectrochemical properties. This study opens an unexplored path for understanding and engineering surface energetics via tuning the surface termination/composition of multinary oxide photoelectrodes.**

Photoelectrochemical water splitting presents an attractive strategy to produce hydrogen gas as an alternative clean fuel in an environmentally benign and sustainable manner<sup>1–3</sup>. The key component of a photoelectrochemical cell is a semiconductor electrode (photoelectrode) that absorbs solar light to generate, separate and transport charge carriers to the semiconductor–electrolyte interface to participate in desired chemical reactions<sup>4</sup>. The electron–hole separation and interfacial charge transfer of the photoelectrode are considerably affected by the interfacial energetics between the photoelectrode and the electrolyte, and/or between the photoelectrode and the buffer, protection or catalyst layers<sup>3,5–9</sup>; hence, the interfacial properties of a photoelectrode are as important as the bulk properties of the photoelectrode.

Strategies for altering the atomic arrangement at the photoelectrode surface that do not involve extrinsic doping have so far mainly involved exposing different semiconductor surface facets<sup>10,11</sup>; however, for ternary oxide photoelectrodes with a formula of A<sub>x</sub>B<sub>y</sub>O<sub>z</sub>, there exist numerous ways to terminate the surface even for the same facet. For example, the surface can be terminated with A–O or B–O, and the surface A:B ratio may be different from the bulk A:B ratio. In fact, if not grown as single crystals, A<sub>x</sub>B<sub>y</sub>O<sub>z</sub> photoelectrodes can have an A- or B-rich surface depending on the synthesis method, which can affect their photoelectrochemical properties. However, despite being important and ubiquitous, the effects of surface termination/composition on a ternary oxide photoelectrode have not been systematically studied and the atomic origin of their effects on interfacial energetics and photoelectrochemical properties have not been elucidated. This lack of study can be attributed to the fact that gaining such a microscopic understanding requires tightly integrated experimental–computational studies that must

meet numerous requirements to obtain meaningful and reliable results as summarized below.

First, samples with at least two different, well-defined surface compositions/structures must be prepared as electrodes. These electrodes must have the same bulk composition/structure/orientation so that any differences observed in the surface energetics and photoelectrochemical properties are solely due to the differences in the surface atom compositions/structures. Furthermore, the difference in composition must only be in the surface atomic layers, and the formation of a thick surface layer of binary oxides of A or B (that is, heterojunctions of A<sub>x</sub>B<sub>y</sub>O<sub>z</sub>/A<sub>m</sub>O<sub>n</sub> or A<sub>x</sub>B<sub>y</sub>O<sub>z</sub>/B<sub>m</sub>O<sub>n</sub>) must be avoided. Moreover, the photoelectrodes should have high photoelectrochemical activity and generate a considerable and reproducible photocurrent so that the difference in photocurrent arising from the difference in surface termination/composition can be unambiguously quantified. Second, realistic surface models that represent the experimental surfaces must be established using a proper level of theory that is capable of accurately describing the surface electronic properties. Third, a procedure must be established to confirm that the surfaces modelled theoretically closely mimic the experimental surfaces. This is not a trivial task; in principle, a plethora of choices for the theoretically modelled surface structure are possible. Fourth, the theoretically predicted and experimentally measured surface energetics must be compared, and the results should closely match to validate the level of theory and the quality of the experimental samples. Finally, the differences in the surface energetics of the samples should be able to explain the differences in the photoelectrochemical properties of the samples.

Here we report a study designed to meet all of the aforementioned requirements. BiVO<sub>4</sub> is chosen as a model ternary oxide

<sup>1</sup>Department of Chemistry, University of Wisconsin–Madison, Madison, WI, USA. <sup>2</sup>Pritzker School of Molecular Engineering, University of Chicago, Chicago, IL, USA. <sup>3</sup>Center for Functional Nanomaterials, Brookhaven National Laboratory, Upton, NY, USA. <sup>4</sup>Department of Materials Science and Chemical Engineering, Stony Brook University, Stony Brook, NY, USA. <sup>5</sup>Department of Chemistry, University of Chicago, Chicago, IL, USA. <sup>6</sup>Argonne National Laboratory, Lemont, IL, USA. <sup>7</sup>These authors contributed equally: Dongho Lee, Wennie Wang, Chenyu Zhou. ✉e-mail: [mzliu@bnl.gov](mailto:mzliu@bnl.gov); [gagalli@uchicago.edu](mailto:gagalli@uchicago.edu); [kschoi@chem.wisc.edu](mailto:kschoi@chem.wisc.edu)

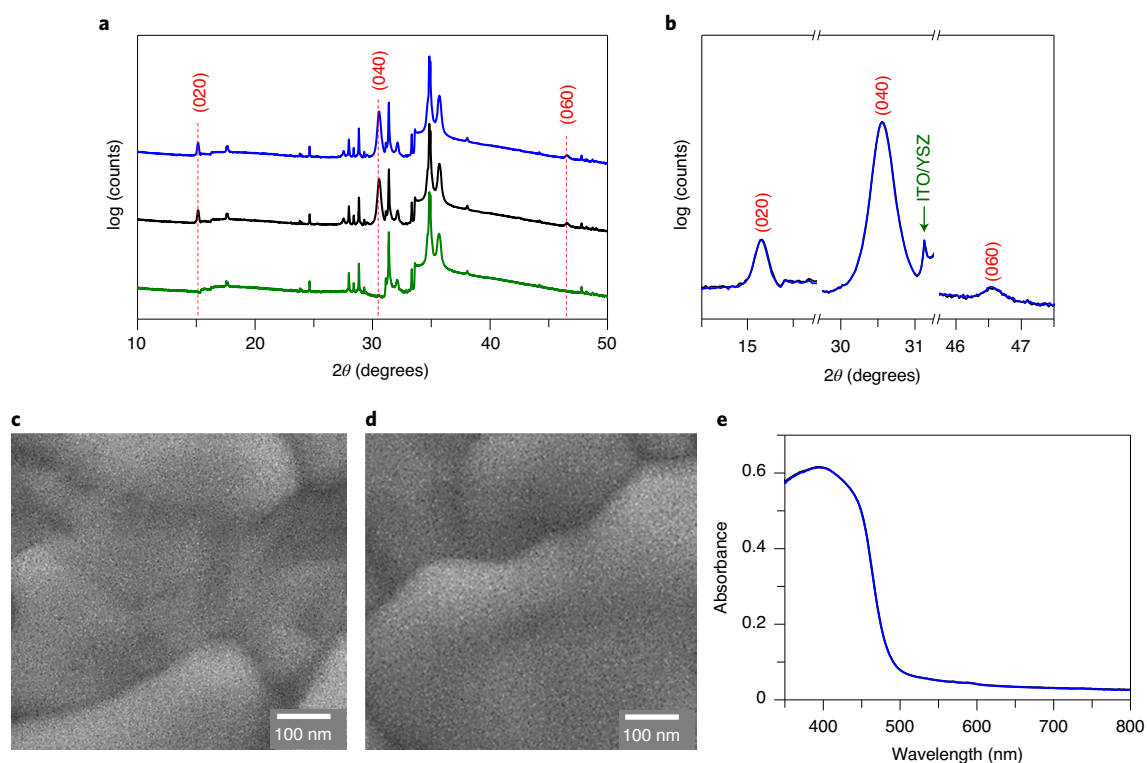


**Fig. 1 | Characterization of epitaxial  $\text{BiVO}_4$  (010) electrodes.** **a**, X-ray diffraction patterns of as-prepared (black) and base-treated (blue) epitaxial  $\text{BiVO}_4$  electrodes (JCPDS 14-0688). An X-ray diffraction pattern of the ITO/YSZ substrate is shown in green and (0k0) peaks are marked in red. **b**, Magnifications of the (0k0) diffraction peaks in **a**. **c,d**, Top-view SEM images of as-prepared (**c**) and base-treated (**d**) epitaxial  $\text{BiVO}_4$  electrodes. **e**, Ultraviolet-visible spectra of as-prepared (black) and base-treated (blue) epitaxial  $\text{BiVO}_4$  electrodes. In **b** and **e**, only the blue lines may be visible because the black lines coincide exactly with the blue lines.

photoelectrode as it has been identified as the most promising oxide photoelectrode for photoelectrochemical water splitting<sup>4,12–15</sup>. We studied epitaxially grown  $\text{BiVO}_4$  (010) photoelectrodes with vanadium- and bismuth-rich exposed facets. We also computationally modelled vanadium- and bismuth-rich (010) facets using first-principles calculations whose simulated scanning tunnelling microscopy (STM) images match well with the experimental ones. Using well-defined experimental samples and matching surface structural models, here we provide a comprehensive computational and experimental interpretation of the effects of surface termination/composition on the interfacial energetics and photoelectrochemical properties of  $\text{BiVO}_4$  (010) photoelectrodes.

### Characterization of the epitaxial $\text{BiVO}_4$ electrodes

The  $\text{BiVO}_4$  films used in this study were epitaxially grown by pulsed laser deposition on an yttrium-stabilized cubic zirconia (YSZ) substrate coated with a thin epitaxial layer of indium tin oxide (ITO), which makes the substrate electrically conductive<sup>16</sup>. The X-ray diffraction (XRD) pattern of the resulting  $\text{BiVO}_4$  film shows only (0k0) peaks (Fig. 1a,b), confirming that the film has uniformly grown along the [010] direction. The *hkl* indices used are with respect to the C-centred monoclinic cell (C 2/c; see Supplementary Fig. 1)<sup>12</sup>. The surface Bi:V ratio of the as-prepared electrode was examined using low-energy ion scattering spectroscopy (LEIS), whose sampling depth is limited to the sample's first atomic layer<sup>17,18</sup>. The surface Bi:V ratio was 43:57, which is slightly vanadium rich.

To change the atomic termination and prepare a bismuth-rich surface of  $\text{BiVO}_4$ , we treated the as-prepared  $\text{BiVO}_4$  with base (0.1 M NaOH) for 1 min. This process takes advantage of the fact that vanadium on the surface of  $\text{BiVO}_4$  more readily leaches out in

basic solution<sup>19</sup>. The goal of the base treatment was to remove only the outermost vanadium layer without altering the bulk. The concentration of base and the time of immersion were thus carefully optimized to achieve this goal. After the optimized base treatment, the surface Bi:V ratio was determined to be 79:21 by LEIS. The Bi:V ratio measured by X-ray photoelectron spectroscopy (XPS) was 53:47. As XPS has a sampling depth that is deeper than the first atomic layer, the Bi:V ratio determined by XPS is the average Bi:V ratio of the first atomic layer and the next few underlying atomic layers. The fact that the Bi:V ratio measured by XPS is still very close to the stoichiometric 1:1 ratio demonstrates that the base treatment eliminated only the surface vanadium atoms while maintaining the stoichiometric Bi:V ratio in the underlying bulk layers.

Top-view scanning electron microscopy (SEM) images (Fig. 1c,d) and electrochemically active surface areas of the electrodes before and after the base treatment (Supplementary Fig. 2) were examined to ensure that the base treatment did not change the surface morphology or roughness; they were found to be comparable. Furthermore, XRD patterns showed no changes in peak height and width (Fig. 1a,b), and ultraviolet-visible spectra showed no changes in absorbance (Fig. 1e) before and after the base treatment, which further confirmed that the base treatment did not alter the bulk properties of the  $\text{BiVO}_4$  electrodes.

### Surface atomic structure with measured and simulated STM

Further direct evidence that the base treatment successfully altered the surface termination of the epitaxial  $\text{BiVO}_4$  electrode was obtained by STM. The STM images of the as-prepared and base-treated samples are shown in Fig. 2b,c, along with the lattice spacing on the (010) plane from the crystallographic data of

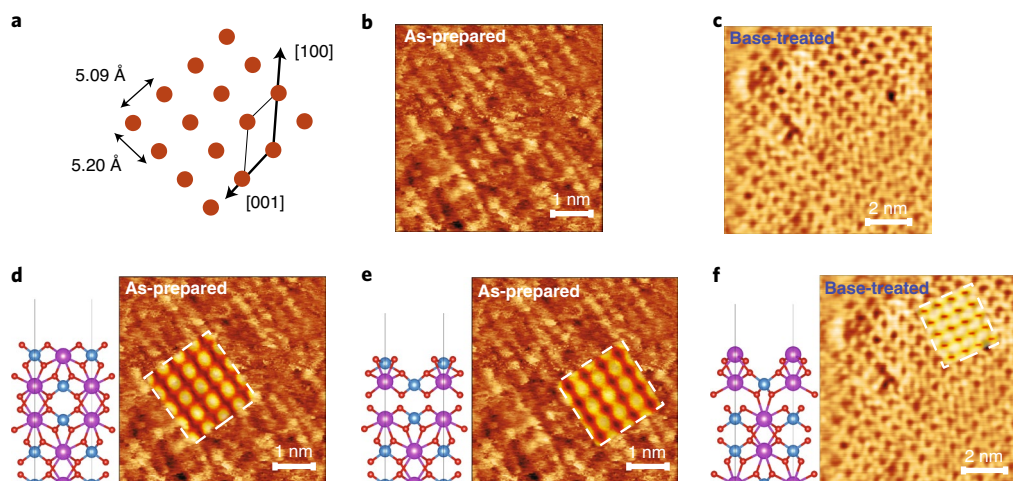


**Fig. 2 | Experimental and simulated STM images of  $\text{BiVO}_4$  (010).** **a**, A schematic of the (010) in-plane lattice of  $\text{BiVO}_4$  oriented with respect to the lattice in the STM images, showing lattice spacing and the C2/c cell convention. **b,c** Measured constant current STM images of the unoccupied states for the as-prepared (**b**) and base-treated (**c**)  $\text{BiVO}_4$  (010) surface. **d–f**, The simulated constant current STM images of stoichiometric (**d**), vanadium-rich (**e**) and bismuth-rich (**f**) surfaces overlaid (enclosed within white dashed lines) on the measured STM images. The corresponding stoichiometric, vanadium- and bismuth-rich slab structures used for the simulations are shown on the side. Purple, bismuth; blue, vanadium; red, oxygen.

$\text{BiVO}_4$  (Fig. 2a). It is apparent that the surface features of the two samples are markedly different. The STM image of the as-prepared sample shows distinct rows of uniformly spaced round features. The spacing between bright spots ranges between 4.5 and 5.5 Å, which is comparable with the lattice spacing in the (010) plane (Fig. 2a). Representative height profiles are provided in Supplementary Fig. 3; the height difference varies between 0.4 and 0.7 Å.

The STM image for the base-treated sample (Fig. 2c) also shows uniformly spaced features, but the bright regions are not round in shape. The distance between the repeating units ranges between 5.0 and 6.0 Å, again close to the lattice spacing in the (010) plane. The difference in height between bright and dark regions varies between 0.8 and 1.1 Å (Supplementary Fig. 4).

We next compared our measured STM images with those simulated using density functional theory (DFT). The surface termination models with simulated STM images that closely resemble the measured STM images are shown in Fig. 2d–f. More details for determining and choosing these surface models as well as their structural descriptions are provided in the Methods.

For the as-prepared sample, we compared the measured STM image with simulated images of the stoichiometric and vanadium-rich surfaces (Fig. 2d,e). Both surfaces exhibit the same uniformly spaced bright features, which predominantly correspond to the surface vanadium atoms (see Supplementary Fig. 5 for the layer-by-layer decomposition of the local density of states at the surface). The spacing of the rounded features coincides with the lattice spacing of the simulation cell, thus allowing us to align the simulated and measured STM images. Both simulated STM images using the stoichiometric and vanadium-rich surface seem comparable with the measured STM image of the as-prepared sample. In our calculations, the height difference between bright and dark regions of the stoichiometric surface is 0.56 Å, which lies comfortably within the range of measured height profiles (0.4–0.7 Å); in the vanadium-rich surface, that height difference is 1.4 Å. In terms of a height profile, the stoichiometric model thus provides a better fit, which agrees with the LEIS result showing that the as-prepared sample is only slightly vanadium rich.

We next compared the measured STM image of the base-treated bismuth-rich sample with a simulated STM image of our bismuth-rich surface model (Fig. 2f). The bright features

predominantly correspond with the unoccupied oxygen 2p states that emerge as in-gap defect levels in our calculations (Supplementary Fig. 5). The spacing and shape of the pattern in the simulated image again match well with those in the observed image. Notably, the height difference between bright and dark regions in our calculated STM image is 1.23 Å, which is in good agreement with measurements (0.8–1.1 Å). From our structural model of the bismuth-rich surface, we see that these deeper regions come from the etching of surface vanadium atoms.

The excellent agreement between the measured and simulated STM images confirms that we successfully prepared epitaxial electrodes with vanadium- and bismuth-rich terminations. These results also confirm that our calculations use representative structural models that closely mimic the surface features of real experimental samples. We are hence now in a position to discuss the electronic structure of validated surface structural models and compare with experimental results to reveal the effect of different surface terminations on surface electronic structure.

### Electronic structures and surface energetics

In our earlier study on the  $\text{BiVO}_4$  (010) surface<sup>20</sup>, we demonstrated excellent agreement of the band alignment and work function between our calculations of the stoichiometric (010) surface and the measurements on single crystalline samples reported in a previous study<sup>21</sup>. In this study we used DFT with a Hubbard term U to compare surface terminations at the (010) surface as previous studies have demonstrated that DFT+U captures the overall physics of high levels of theory (that is, hybrid functionals<sup>20,22</sup>).

Band-edge positions of vanadium- and bismuth-rich structures were calculated using the aforementioned surface models (100% vanadium-rich and 100% bismuth-rich surfaces) and compared with those of calculated and experimental stoichiometric (that is, single-crystal) surfaces in Fig. 3. Although experimental vanadium- and bismuth-rich samples do not exhibit complete loss of bismuth or vanadium on the surface, our chosen structural models allow us to understand the maximal difference in electronic structure among different surface terminations and provide meaningful atomistic insights. The greatest change in the band-edge position for the vanadium-rich surface is the valence band maximum (VBM), which moves up by about 0.4 eV relative to the stoichiometric surface.

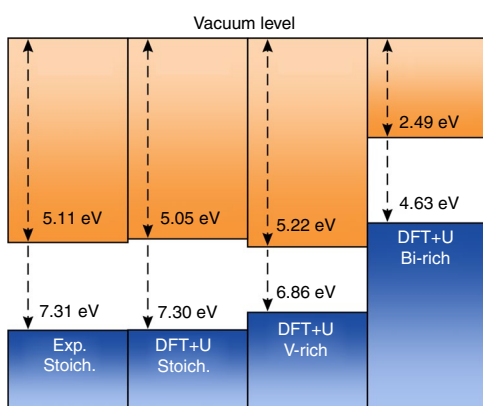


**Fig. 3 | Band alignments of BiVO<sub>4</sub> (010).** Results obtained from calculations at the DFT+U level for the BiVO<sub>4</sub> (010) surface with stoichiometric (stoch.), vanadium- and bismuth-rich terminations compared with the experimental results obtained from single-crystal BiVO<sub>4</sub> (010) samples<sup>21</sup>. Generated with the help of bapt (<https://github.com/utf/bapt>).

The bismuth-rich surface exhibits a larger shift in the band-edge positions towards the vacuum level relative to the stoichiometric surface. Varying the surface bismuth richness almost linearly affects the magnitude of the band edge shift (Supplementary Fig. 6). We note that our results were obtained with surface models with a limited slab size and particular choice of surface bismuth coordination (see Methods for the choice of oxygen surface coordination); thus, our results do not intend to exactly predict the band-edge positions of the experimental samples, but are instead meant to present and explain the trend that the band-edge positions shift towards the vacuum level as the surface bismuth content increases in comparison with those of the stoichiometric or vanadium-rich sample. The VBM of stoichiometric BiVO<sub>4</sub> is sufficiently more positive (that is, farther from vacuum) than the water oxidation potential and therefore the shift of the band edges towards the vacuum level is favourable for overall water splitting as long as the VBM is more positive with respect to the water oxidation potential.

The difference in band-edge positions among the stoichiometric, vanadium- and bismuth-rich surfaces can be explained using computed average electrostatic potentials ( $\bar{V}$ ). The calculation of electrostatic potentials to align energy levels of surface structural models is a well-established technique in semiconductor physics<sup>23,24</sup>. Energy levels in slabs with different stoichiometries do not have a common zero of energy in our calculations. The average electrostatic potentials felt by the electrons in the bulk-like region of the slabs used to model each surface were computed (dotted lines in Fig. 4) and aligned relative to vacuum to compare these energy levels.

The depth of the average electrostatic potential with respect to vacuum corresponds to the strength of the potential that the electrons experience in the slab. The large shift in band-edge positions of the bismuth-rich surface towards the vacuum level can thus be understood as mostly arising from the shift in the average electrostatic potential towards the vacuum level. The overall determination of the band-edge positions of course includes the details of the surface relaxations and resulting electronic structure (Supplementary Fig. 5).

The electrostatic potential of the electrons within each slab exhibits variations at the atomic level due to the charge variation around atoms and in bonds. The variation in  $\bar{V}$  along the direction perpendicular to the surface (that is, [010]) is referred to as the macroscopic electrostatic potential and is represented by the solid lines in Fig. 4. We note that the macroscopic electrostatic potential for the vanadium-rich slab at the surface exhibits a well at a lower potential compared with that in the bulk-like region (orange arrows

in Fig. 4, 0.98 eV). A similar potential well exists (black arrows in Fig. 4, 0.68 eV) at the surface of the stoichiometric slab and is a consequence of the structural surface relaxations of the (010) surface in BiVO<sub>4</sub> (ref. 20). The presence of a potential well indicates that electrons tend to accumulate at the surface. A shallower potential well exists at the surface of the bismuth-rich slab relative to the bulk region (blue arrows in Fig. 4, 0.46 eV), indicating that the depth of the well is largely affected by the presence of surface vanadium and associated surface structural relaxations. The change in  $\bar{V}$  as the function of surface bismuth richness can be found in Supplementary Fig. 7.

The differences in electronic structure of the stoichiometric, vanadium- and bismuth-rich surfaces have several important implications for the photoelectrochemical properties of the (010) surface of BiVO<sub>4</sub>. First, our results show that changing the surface termination/composition of the facet can have a considerable effect on the band alignment even without modifying the atomic planes exposed on the surface. This is an important insight as such effects would have previously been expected only by exposing a different facet on the surface<sup>10,11</sup>. Figures 3 and 4 suggest that the base-treated sample with a higher Bi:V ratio can possess a conduction band minimum and VBM that are shifted closer to the vacuum level and can have a more favourable band alignment for overall photoelectrochemical water splitting as long as the VBM position remains suitable for water oxidation. Second, the smaller concentration of surface vanadium of the base-treated sample may result in fewer recombination events. It has been reported that electron polarons tend to form on vanadium sites<sup>20,25</sup>, whereas hole polarons tend to form on bismuth sites<sup>26,27</sup>. Thus, by virtue of having fewer vanadium sites and a shallower potential well, the bismuth-rich surface has less tendency for electron polarons to form and recombine with the hole polarons needed for water oxidation.

We next examined the effect of surface termination on the work function. The calculated work function of the stoichiometric surface is 5.36 eV, which compares well to the measured work function (5.15 eV) of a single-crystalline BiVO<sub>4</sub> doped with ~1 at% molybdenum substitutionally for vanadium<sup>21</sup>. We obtained a work function of 6.63 eV for the vanadium-rich surface and 4.06 eV for the bismuth-rich surface. As our vanadium-rich surface is constructed with total loss of bismuth in the top layer and our bismuth-rich surface is with total loss of vanadium in the top layer, our calculated work functions represent two extreme deviations from the stoichiometric one. The work function of samples with intermediate loss of surface atoms will thus be between these two extreme values, with the trend that a high surface Bi:V ratio would shift the work function closer to the vacuum level. We note that the surface slabs were modelled as intrinsic semiconductors with no excess carriers in these calculations. The changes in work function solely originate from the shift of the band edges and from details of the electronic structure of the relaxed slab structure, which affect the density of states and the presence of interband states (Supplementary Fig. 5). These results are therefore not meant to precisely predict the work function of experimental n-type BiVO<sub>4</sub> samples but to show the effect of the surface Bi:V ratio on the work function even in the absence of any change in the carrier density. Overall, our computational results for the band-edge positions and work functions predict that the bismuth-rich surface will be able to achieve a more favourable band bending at the BiVO<sub>4</sub>-electrolyte interface and enhanced electron-hole separation.

We measured the work functions and VBMs of as-prepared and base-treated samples using XPS to examine whether the trends observed computationally are also observed experimentally (Supplementary Fig. 8). The work functions of the as-prepared and base-treated samples are 4.80 eV and 4.40 eV, respectively, whereas the VBMs are 6.38 eV and 6.23 eV, respectively. These results show that the base-treated samples possess a work function

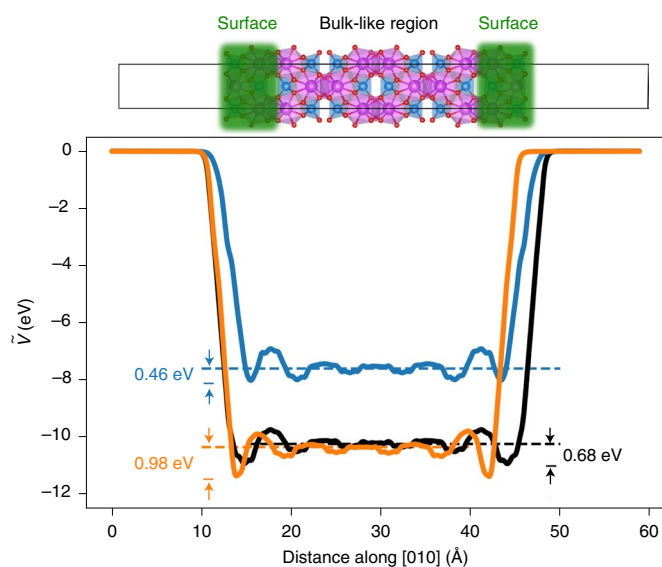


**Fig. 4 | Calculated macroscopic  $\bar{V}$  of  $\text{BiVO}_4$  (010).** Values of  $\bar{V}$  (solid lines) for stoichiometric (black), bismuth-rich (blue), and vanadium-rich (orange) slabs following the structural models in Fig. 2. A generic slab structure for  $\text{BiVO}_4$  is shown above, indicating the corresponding surface and bulk-like regions in  $\bar{V}$ . The black, blue and orange dashed lines indicate  $\langle \bar{V} \rangle$  in the bulk-like region for the stoichiometric, bismuth-rich and vanadium-rich slab structures, respectively. The arrows indicate the depth of the potential difference between  $\bar{V}$  of the surface and of the bulk-like region for each slab structure. The null is taken as the vacuum level.

and VBM shifted closer to the vacuum level compared with those of the as-prepared ones, which is the trend predicted by our calculations (as explained previously, the calculated and experimental work functions and VBM positions are not expected to match exactly). We confirmed via XPS that the core level bismuth and vanadium peaks do not show any chemical shifts after base treatment (Supplementary Fig. 9). The observed changes are thus due to the base treatment affecting only the surface Bi:V ratio and not the oxidation states of surface bismuth and vanadium ions. Both the computational and experimental results consistently suggest that altering the surface termination of the same facet has a considerable impact on the interfacial energetics of  $\text{BiVO}_4$  and that the bismuth-rich (010) surface is more favourable for solar water splitting.

### Photoelectrochemical properties

To investigate how different atomic terminations of  $\text{BiVO}_4$  (010) affect the photoelectrochemical properties,  $J$ - $V$  plots for sulfite oxidation of as-prepared and base-treated samples were measured in 0.5 M borate buffer containing 0.4 M  $\text{Na}_2\text{SO}_3$  under air mass 1.5 global (AM 1.5 G), 100  $\text{mW cm}^{-2}$  illumination (Fig. 5a). Sulfite is a hole scavenger with fast interfacial oxidation kinetics<sup>7,28,29</sup>. The surface recombination of holes can thus be assumed to be negligible. As a result, the photocurrent onset potential can reasonably be equated to the flatband potential ( $E_{\text{FB}}$ ) of  $\text{BiVO}_4$  (ref. 29). Furthermore, the difference in photocurrent between the two types of samples can be directly related to the difference in the number of surface-reaching holes, which results from the effect of surface termination on interfacial energetics and band bending<sup>29</sup>.

We measured  $J$ - $V$  plots of six as-prepared and six base-treated samples (Supplementary Fig. 10); the averaged  $J$ - $V$  plots with standard deviations are shown in Fig. 5a. As these two sets of samples

are identical except for the surface termination, the observed differences must be solely due to the different surface terminations. The results show that the base-treated samples consistently showed significantly higher photocurrent than the as-prepared samples (Fig. 5a). Furthermore, the average photocurrent onset potential (or the average  $E_{\text{FB}}$ ) of the base-treated samples ( $0.24 \pm 0.03$  V versus RHE) is shifted in the negative direction compared with that of the as-prepared samples ( $0.41 \pm 0.06$  V versus RHE). This result agrees well with the XPS results showing that the work function of the base-treated sample shifted closer to the vacuum. The difference in the  $E_{\text{FB}}$  values (0.17 V) is not exactly the same as the difference in the work functions measured with XPS (0.40 eV); however, we note that the differences in  $E_{\text{FB}}$  and work function do not need to be the same as  $E_{\text{FB}}$  is affected not only by the work function but also by the Helmholtz layer potential drop ( $V_{\text{H}}$ ) at the photoelectrode-electrolyte interface (see Methods for details). With this understanding, the results shown in Fig. 5a agree well with computationally and experimentally determined energetics of the vanadium- and bismuth-rich  $\text{BiVO}_4$  (010) photoelectrodes; the band-edge positions and work function of the bismuth-rich surface are closer to vacuum and result in more band bending at any given potential, thus producing more surface-reaching holes. These results clearly demonstrate that altering the surface composition can result in a considerable difference in photocurrent generation.

As the  $J$ - $V$  measurements may change the surface Bi:V ratio and therefore change the surface energetics, we repeated the measurements and examined the corresponding changes in the Bi:V ratio, VBM and work function of both samples. For the as-prepared sample, the photocurrent onset gradually shifted in the negative direction and the photocurrent continually increased until convergence was reached after the seventh measurement (Fig. 5b). The LEIS and XPS analysis after the first and eighth  $J$ - $V$  measurements revealed that the observed changes were due to the loss of surface vanadium during the measurements, converting the vanadium-rich surface to a bismuth-rich surface (Supplementary Table 1). The most drastic loss of vanadium occurred during the first  $J$ - $V$  measurement with the surface Bi:V ratio changing from 43:57 to 79:21; the surface eventually reached an equilibrium Bi:V ratio at pH 9.3, as indicated by the convergence of the  $J$ - $V$  plot after the seventh measurement. The increase in the surface Bi:V ratio also affected the VBM and work function positions; both shifted towards the vacuum level (Supplementary Table 1), as expected from our calculations. The base-treated sample also showed a slight increase in the surface Bi:V ratio during the  $J$ - $V$  measurements from 79:21 to 86:14; however, the change in the surface Bi:V ratio and the positions of VBM and work function were considerably less than those observed for vanadium-rich samples. The  $J$ - $V$  plots also showed a corresponding small increase in photocurrent; the plots converged after the second measurement (Fig. 5c). In summary, the LEIS and XPS analyses performed after the  $J$ - $V$  measurements of both samples consistently indicate that the surface Bi:V ratio is a key factor affecting the surface energetics and photocurrent generation of  $\text{BiVO}_4$ , even if the two  $\text{BiVO}_4$  surfaces may undergo further unique surface reconstructions in water (for example, dissociative water adsorption) and during  $J$ - $V$  measurements. The effects of the surface Bi:V ratio on the surface reconstruction of  $\text{BiVO}_4$  will be investigated in our future study.

### Conclusions

In summary, we performed combined experimental and computational investigations using epitaxial  $\text{BiVO}_4$  (010) photoelectrodes with vanadium- and bismuth-rich facets and matching surface structural models to understand the impact of surface composition on their interfacial energetics and photoelectrochemical properties. We obtained coherent experimental and computational results that provide atomistic insights into the relationship between

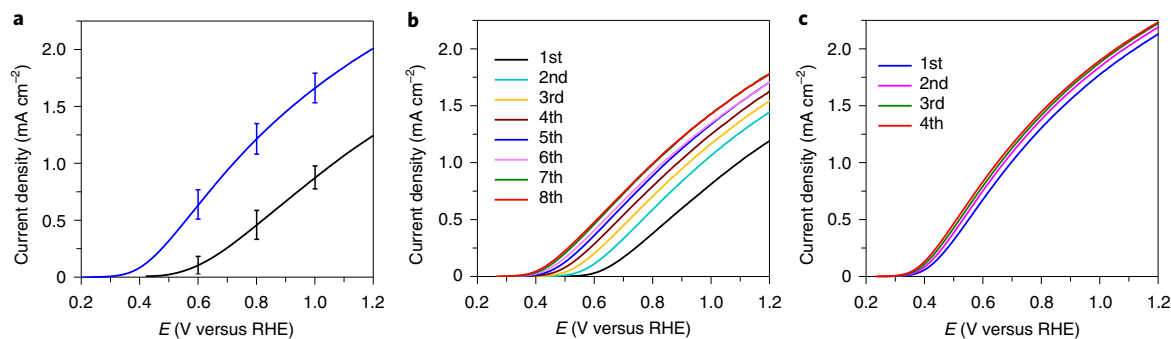


**Fig. 5 | Photoelectrochemical properties of epitaxial BiVO<sub>4</sub> (010) electrodes.** **a**, *J*-*V* plots for sulfite oxidation of as-prepared (black) and base-treated (blue) BiVO<sub>4</sub> electrodes; each curve is obtained by averaging the *J*-*V* plots of six individual samples. The error bars represent the standard deviations of the average current densities at selected potentials. The *J*-*V* plots were recorded in 0.5 M borate buffer (pH 9.3) containing 0.4 M Na<sub>2</sub>SO<sub>3</sub> under AM 1.5 G, 100 mW cm<sup>-2</sup> illumination. **b,c**, Repeated *J*-*V* measurements of the as-prepared (**b**) and base-treated (**c**) BiVO<sub>4</sub> electrodes under the same conditions.

surface termination/composition and photoelectrochemical properties. Our results unambiguously show that the surface Bi:V ratio is a key factor affecting the band-edge position and work function: as the surface bismuth content increases, these positions shift towards the vacuum level. As a result, the bismuth-rich surface has more favourable surface energetics for overall solar water splitting and also produces a higher photocurrent density at any given bias. We found that the changes in the surface Bi:V ratio during photocurrent measurements correlate well with the changes in the band-edge positions, work function and photocurrent generation. Our study represents a critical advancement towards the microscopic understanding of the effect of surface composition in ternary oxide photoelectrodes on their photoelectrochemical properties. We plan to build our understanding of the interfacial energetics of vanadium- and bismuth-rich BiVO<sub>4</sub> (010) further by examining the effect of water and an oxygen evolution catalyst on the surface of BiVO<sub>4</sub> in our future studies.

## Methods

**Synthesis of epitaxial BiVO<sub>4</sub> electrodes.** Epitaxial BiVO<sub>4</sub> thin films were deposited on YSZ (010) single-crystalline substrates (MTI Corp.) by pulsed laser deposition using a KrF excimer laser ( $\lambda = 248$  nm) operated at a repetition rate of 20 Hz and a fluence of 1.8 J cm<sup>-2</sup>. The BiVO<sub>4</sub> laser ablation target was prepared by a conventional ceramic sintering method using commercially available BiVO<sub>4</sub> powder (Alfa Aesar, 99.9%, ~200 Mesh). To prepare the target, the BiVO<sub>4</sub> powder was ground further in an alumina mortar and pressed into a pellet of 30 mm diameter and 5 mm thickness. Finally, the pellet was calcined in air at 700 °C for 10 h to produce the BiVO<sub>4</sub> pulsed laser deposition target. For photoelectrochemical and STM characterizations, a 50-nm-thick ITO film was first deposited over the YSZ substrate at 600 °C under a base pressure of  $6 \times 10^{-7}$  Torr to make the substrate electrically conducting; BiVO<sub>4</sub> films were subsequently deposited at 625 °C in 20 mTorr of oxygen. The target-to-substrate distance was maintained at 6 cm. After deposition, the films were cooled down to room temperature under the same atmosphere at a rate of 10 °C min<sup>-1</sup>. Under these deposition conditions, BiVO<sub>4</sub> films grow along the [010] direction and expose the (010) atomic plane on the surface. The epitaxial nature of the resulting BiVO<sub>4</sub> (010) films was confirmed in our previous study by atomic resolution high angle annular dark field scanning transmission electron microscopy and selected area electron diffraction<sup>16</sup>. The crystallographic axes used in this study are based on the C-centred monoclinic cell (C 2/c)<sup>12</sup>.

**Surface treatment of BiVO<sub>4</sub> electrodes.** To create a bismuth-rich surface, the as-prepared BiVO<sub>4</sub> electrode was immersed in 15 ml of 0.1 M NaOH (Sigma-Aldrich, 97%) aqueous solution for 1 min to strip surface vanadium atoms (this condition was optimized for the BiVO<sub>4</sub> electrodes used in this study). The base-treated electrodes were rinsed with deionized water (Barnstead E-pure water purification system, resistivity >18 MΩ cm) and blow-dried with air.

**Characterization.** Scanning tunnelling microscopy images were collected from as-prepared and base-treated BiVO<sub>4</sub> electrodes using an ultra-high vacuum (UHV)-STM (RHK-7500) with a tungsten tip. Before scanning over the BiVO<sub>4</sub> samples, the tungsten tip was pre-treated by repeatedly scanning over Au(111).

The images were acquired at room temperature under UHV ( $\sim 10^{-10}$  torr) at positive bias (electron tunnelling from tip to BiVO<sub>4</sub> unoccupied states in sample) up to 2.0 V in constant current mode. Scanning at negative bias (electrons tunnelling from BiVO<sub>4</sub> occupied states to tip) was also carried out but could not produce high-resolution images due to the difficulty in maintaining a stable tunnelling current without crashing the tip onto the sample. The failure of image acquisition at negative bias suggests that there are not enough electrons available in occupied states for tunnelling into the tip. Scanning tunnelling microscopy images were post-processed using Gwyddion software (v.2.54, <http://gwyddion.net/>)<sup>30</sup>.

The morphology of the BiVO<sub>4</sub> electrodes was examined using SEM (LEO 1530 microscope, Gemini) at an accelerating voltage of 5 kV. The crystallinity and growth orientation of the electrodes were confirmed with XRD (D8 Advance X-ray diffractometer, Bruker) using nickel-filtered copper K $\alpha$ -radiation with  $\lambda = 1.5418$  Å. The optical absorbances of the electrodes were determined using a Cary 5000 ultraviolet-visible-near infrared spectrophotometer (Agilent) with an integrating sphere to simultaneously collect reflectance and transmittance from the electrodes. The VBM and work function of the electrodes were investigated by XPS (K $\alpha$  X-ray photoelectron spectrometer, Thermo Scientific) using monochromatized aluminium K $\alpha$  X-ray (1,486.68 eV) as the excitation source. Silver metal was deposited onto the BiVO<sub>4</sub> electrode using a Hummer 8.3 DC/RF Sputter System (Anatech USA) to make electrical contact with the electrode. The Fermi edge of the argon-ion-beam-cleaned silver metal was used as a reference to calibrate the binding energies of the samples. A negative sample bias of -30 V was applied to determine the secondary electron cutoff, the work function and the  $E_F - E_{\text{VBM}}$  of the BiVO<sub>4</sub> electrodes. Core level XPS spectra were measured with a pass energy of 30 eV and the surface atomic percentages of the bismuth and vanadium were determined from the integrated bismuth 4*f* and vanadium 2*p* peak areas using Avantage software (Thermo Scientific v.5.9919, [https://xpssimplified.com/avantage\\_data\\_system.php](https://xpssimplified.com/avantage_data_system.php)).

**LEIS.** The surface Bi:V ratios of the BiVO<sub>4</sub> electrodes were quantified using LEIS with a SPECS IQE 12/38 ion source and a SPECS Phoibos 100 energy analyser in a UHV chamber. The primary ion is He<sup>+</sup> at a kinetic energy of 1.5 keV, and the scattering angle was fixed at 135°. In LEIS, only the outermost atomic layer significantly contributes to the flux of scattered ions<sup>31</sup>. The kinetic energy of scattered ion ( $E_s$ ) is given by the following equation using the elastic, two-body collision approximation<sup>32</sup>:

$$E_s = E_0 \left( \frac{\cos\theta \pm \sqrt{(M_2/M_1)^2 - \sin^2\theta}}{1 + M_2/M_1} \right)^2 \quad (1)$$

in which  $E_0$  is the kinetic energy of the primary ion (1.5 keV),  $\theta$  is the scattering angle (135°), and  $M_1$  and  $M_2$  are the mass of the primary ion (He<sup>+</sup>) and the surface atom (for example, bismuth or vanadium), respectively. Using equation (1), the  $E_s$  values for bismuth and vanadium were determined to be 1,405 eV and 1,147 eV, respectively. Actual measurements on BiVO<sub>4</sub> samples confirmed these values.

The scattered ion flux corresponding to each metal ( $M$ ),  $S_M$ , is calculated on the basis of the LEIS peak area, which is further used to calculate the surface atomic coverage ratio<sup>17</sup>. It has been established that for each element  $M$ , its surface coverage  $\theta_M$  is proportional to its LEIS scattering flux,  $S_M$ , when the matrix effect is negligible<sup>18</sup>, that is,

$$\theta_M = \rho_M S_M \quad (2)$$

where  $\rho_M$  is the LEIS sensitivity factor of element  $M$ . As such, the surface coverage ratio between bismuth and vanadium is given by  $\theta_{\text{Bi}}/\theta_{\text{V}} = \rho_{\text{Bi}} S_{\text{Bi}}/\rho_{\text{V}} S_{\text{V}}$ . As the

value of  $S_{\text{Bi}}/S_{\text{V}}$  is given directly from the LEIS measurement, the sensitivity factor ratio between bismuth and vanadium,  $\rho_{\text{Bi}}/\rho_{\text{V}}$ , needs to be calibrated to determine the surface coverage ratio  $\theta_{\text{Bi}}/\theta_{\text{V}}$ .

To prepare the Bi/V calibration sample, a vanadium foil (Alfa Aesar, 99.8%) was placed in the LEIS chamber and sputtered using argon ions (2 keV, 7  $\mu\text{A}$ ) for 1 h to strip the surface oxide layer. The foil is subsequently annealed under UHV at 400 °C for 1 h to desorb argon atoms from its surface. A pellet of bismuth (Sigma-Aldrich, 99.999%) was placed next to the vanadium foil and cleaned using argon ion sputtering (2 keV, 7  $\mu\text{A}$ ) for 1 h and then heated to 200 °C for 1 h under UHV. At this temperature, bismuth sublimates very slowly and condenses on the surface of vanadium foil, forming a submonolayer of adatoms, as observed by LEIS. The surface coverage of bismuth on the vanadium foil varies depending on the distance to the bismuth source (Supplementary Fig. 11, scheme on the right). The coverage is higher in the area closer to the bismuth source and is much lower in the area far away from it. As the surface of the Bi/V calibration sample is covered with either bismuth or vanadium, the total coverage,  $\theta_{\text{Bi}} + \theta_{\text{V}}$ , equals unity at any point of the sample. Based on equation (2), we have  $\rho_{\text{Bi}}S_{\text{Bi}} + \rho_{\text{V}}S_{\text{V}} = 1$ , which can be further rearranged as

$$S_{\text{Bi}} = \frac{-\rho_{\text{V}}}{\rho_{\text{Bi}}} S_{\text{V}} + \frac{1}{\rho_{\text{Bi}}} \quad (3)$$

Essentially, equation (3) establishes a linear correlation between the LEIS peak areas of bismuth and vanadium, with its slope equalling the negative of the sensitivity factor ratio  $\rho_{\text{V}}/\rho_{\text{Bi}}$ .

Following this analysis, we measured LEIS spectra at three spots along the gradient of bismuth coverage over vanadium foil (Supplementary Fig. 11). Each spot was measured using identical LEIS conditions. As shown in Supplementary Fig. 12, there is a very clear linear correlation between the peak areas of the two elements, which validates the assumption of negligible matrix effect and gives the sensitivity factor ratio  $\rho_{\text{V}}/\rho_{\text{Bi}} = 0.253$  using linear regression<sup>18</sup>. This sensitivity factor ratio was used to determine the surface Bi:V ratio of our BiVO<sub>4</sub> samples.

**Photoelectrochemical characterization.** Photoelectrochemical and electrochemical measurements were carried out in an undivided three-electrode cell using an SP-200 potentiostat (Bio-Logic). BiVO<sub>4</sub> was used as the working electrode, platinum was used as the counter electrode and Ag/AgCl (4 M KCl) was used as the reference electrode (RE). The measured potential versus the RE was converted to potential versus the reversible hydrogen electrode (RHE) using the equation below (NHE is normal hydrogen electrode).

$$E(\text{versus RHE}) = E(\text{versus Ag/AgCl}) + E_{\text{Ag/AgCl}}(\text{RE}) + 0.0591 \text{ V} \times \text{pH} \quad (4)$$

$$(E_{\text{Ag/AgCl}}(\text{RE}) = 0.1976 \text{ V versus NHE at } 25^\circ\text{C})$$

Simulated solar light was generated using an LCS-100 solar simulator (Oriol) equipped with a 150 W xenon arc lamp and an AM 1.5 G filter. An infrared filter (Newport) and a focusing lens were placed between the light source and the electrode, and the intensity of light was calibrated to 1 sun (100 mW cm<sup>-2</sup>) at the back side of the BiVO<sub>4</sub> electrode using a National Renewable Energy Laboratory-certified GaAs reference cell (photovoltaic measurement). Photoelectrochemical  $J$ - $V$  and  $J$ - $t$  measurements were taken in 0.5 M borate buffer solution, which was prepared by dissolving 0.5 M H<sub>2</sub>BO<sub>3</sub> (Sigma-Aldrich, 99.5%) in deionized water and adjusting the pH to be 9.3 using KOH (Sigma-Aldrich, 85%). For sulfite oxidation, 0.4 M Na<sub>2</sub>SO<sub>3</sub> (Sigma-Aldrich,  $\geq 98\%$ ) was added to the 0.5 M borate buffer solution. The photocurrent onset potentials reported in this study are the open circuit potentials of the two BiVO<sub>4</sub> electrodes under AM 1.5 G illumination where the photocurrent density is zero in the given electrolyte.

The  $J$ - $V$  plots of the as-prepared and base-treated BiVO<sub>4</sub> photoelectrodes for water oxidation are provided in Supplementary Fig. 13, where the photocurrent generated by the base-treated sample is also higher than that of the as-prepared sample. We note that the  $J$ - $V$  plots for water oxidation are not as useful as those for sulfite oxidation in studying the effect of the surface composition on surface energetics as the onset potential and photocurrent generation for water oxidation are affected by other factors not directly related to surface energetics (for example, surface catalytic properties, loss of holes to surface recombination).

It was mentioned in the main text that the differences in  $E_{\text{FB}}$  and work function do not need to be the same. This is because  $E_{\text{FB}}$  is affected not only by the work function but also by the Helmholtz layer potential drop ( $V_{\text{H}}$ ) at the photoelectrode/electrolyte interface as shown in equation (5), where  $\phi_{\text{SC}}$  is the work function of the semiconductor and 4.5 V is the scale factor relating the H<sup>+</sup>/H<sub>2</sub> redox level to vacuum<sup>17</sup>;  $V_{\text{H}}$  (in turn) is affected by the solution pH and the point of zero zeta potential (pH<sub>PZZP</sub>) of the photoelectrode (equation (6)). Thus, if the two samples with different surface terminations possess different pH<sub>PZZP</sub> values (and therefore different  $V_{\text{H}}$  values) then their difference in  $E_{\text{FB}}$  can deviate from their difference in work function.

$$E_{\text{FB}}(\text{V versus NHE}) = \phi_{\text{SC}}(\text{in eV}) + V_{\text{H}}(\text{in V}) - 4.5 \text{ V} \quad (5)$$

$$V_{\text{H}} = 0.059 \text{ V} \times (\text{pH}_{\text{PZZP}} - \text{pH}) \quad (6)$$

**Computational methodology.** Our first-principles calculations were based on Kohn–Sham DFT and used the PBE<sup>33</sup> functional, as implemented in Quantum ESPRESSO (v.6.3)<sup>34,35</sup>. We followed the computational methodology of our previous work on the (010) surface<sup>20</sup>, highlighting relevant aspects here. We used norm-conserving pseudopotentials<sup>36,37</sup> with a 90 Ry energy cutoff and a k-point mesh of 4 × 4 × 2 for bulk cells. Forces were converged to less than 1 meV Å<sup>-1</sup>. All calculations were spin-polarized and included a Hubbard term (U)<sup>38</sup> correction, with U = 2.7 eV applied to the *d* electrons of the vanadium sites. Previous studies have demonstrated that the DFT+U approach is appropriate for studying defect physics when properly benchmarked against higher level calculations (that is, calculations using hybrid functionals<sup>25,29</sup> as done in previous work).

To model surfaces, we used symmetric slabs<sup>39</sup> generated with Pymatgen<sup>40</sup> and the Atomic Simulation Environment<sup>41</sup> based on the 24-atom cell and a minimum of eight atomic layers and 20 Å of vacuum. We approximated the monoclinic cell with a tetragonal one for computational convenience; this is a robust approximation as demonstrated in our previous work<sup>20</sup>. The relationship between the I-centred tetragonal cell used for computational study and the C-centred monoclinic cell (C 2/c) of BiVO<sub>4</sub> is shown in Supplementary Fig. 1. We simulated three surface terminations for the (010) surface. The stoichiometric surface shown in Fig. 2d consists of fourfold-coordinated vanadium atoms and sixfold coordinated bismuth atoms. To mimic the bismuth-rich (vanadium-rich) surface, we removed surface vanadium atoms (bismuth atoms) and relaxed the resulting geometry to within 100 meV Å<sup>-1</sup>. We use a 4 × 4 × 1 k-point mesh for 1 × 1 × 2 supercells (72 atoms) and 2 × 2 × 1 k-point mesh for 2 × 2 × 2 supercells (192 atoms). Using 2 × 2 × 2 supercells, we verified that our structural surface models maintain the 1 × 1 surface reconstruction, as observed for the measured stoichiometric (010) surface. Simulated STM images were generated using the framework developed by Tersoff and Hamann<sup>42</sup> as implemented in Quantum ESPRESSO. Among the many possible configurations of BiVO<sub>4</sub> surfaces, we considered the stoichiometric (010) surface, which contains a 1:1 Bi:V ratio and is known to be one of the lowest energy surfaces<sup>43</sup>. We note that in a previous work<sup>20</sup> we showed that using an integrated experimental and theoretical strategy, one can successfully describe the band alignment and work function of the stoichiometric (010) surface (including in the presence of oxygen vacancies).

We then removed the outermost bismuth and vanadium atoms from the surface to obtain the vanadium- and bismuth-rich slab structures, respectively. A further consideration in identifying a structural model for the surface is the coordination of the remaining surface vanadium and bismuth atoms with oxygen; we considered several coordinations of the remaining surface vanadium and bismuth atoms with oxygen by removing the appropriate number of surface oxygen atoms starting from the coordinations present in the stoichiometric surface. In our calculations, we optimized the internal atomic coordinates of all slabs chosen to represent each surface. For the vanadium-rich surface, we considered fourfold and twofold coordinations of the surface vanadium atoms with oxygen. Following relaxation, the twofold coordination of surface vanadium atoms becomes a compressed fourfold coordination. The resulting surface model shown in Fig. 2e corresponds to a simulated STM image that has the best agreement with the measured one.

For the bismuth-rich surface, we considered configurations with fourfold, fivefold and sixfold coordination of the surface bismuth atoms. We found that the sixfold termination of surface bismuth is unstable and the surface bismuth tend to relax to have low oxygen coordinations (for example, fourfold and fivefold configurations). We were able to eliminate the structural model in which all of the surface bismuths are fivefold coordinated on the basis of simulated STM images and band-alignment calculations. The simulated STM image of the fourfold-coordinated surface bismuth provides the best fit to the measured one among the structures considered; the structural model for the fourfold-coordinated bismuth surface and corresponding STM image are shown in Fig. 2f. Nevertheless, as the Bi–O bond is relatively weak, it is plausible that the surface bismuth on the experimental surface has a mixture of various oxygen coordinations. As mentioned in the main text, we use a surface model with only fourfold-coordinated bismuth atoms for the bismuth-rich surface in our calculations. Absolute differences between measured and simulated band-edge positions may be (in part) explained by the more diverse and complex oxygen coordination environments possible in the experimental samples. We note again that our calculations nonetheless predict that the surface Bi:V ratio has a significant impact on the band-edge positions and subsequently the photoelectrochemical properties of BiVO<sub>4</sub> electrodes. We further calculated the change in band-edge alignment with vacuum as a function of surface bismuth content. To simulate surfaces with intermediate bismuth richness, we incrementally removed each surface vanadium atom and any associated oxygen atoms (to maintain a fourfold coordination of the surface bismuth) at each exposed surface. There are four different surface vanadium sites in our 2 × 2 × 2 supercell; we label the removal of one vanadium atom as 25% bismuth-rich, the removal of two vanadium atoms as 50% bismuth-rich, and so on. Our calculations show a linear dependence of the band-edge positions with surface bismuth content (Supplementary Fig. 6).

We require a common energy reference to calculate the band alignment between different slab structures. As such, we calculated the average electrostatic potential of each of our slab structures and aligned them to the vacuum level.

We use the implementation available in the Quantum ESPRESSO package. The electrostatic potential is defined as the sum of the ionic and Hartree potentials, that is, the full electron potential excluding many-body electron interactions captured in the exchange–correlation potential. The electrostatic potential contains fluctuations that correspond to the charge variation due to atoms and bonds in the simulation cell. Thus, we performed a planar average perpendicular to the slab surface and a windowing average to arrive at  $\bar{V}$ . We then determined  $\langle \bar{V} \rangle$  of the slab structure and determined the band alignment among different slab structures.

### Data availability

The dataset generated and analysed in the current study are openly available on Qresp<sup>††</sup> (Qresp.org) through the University of Chicago node; <https://doi.org/10.6084/m9.figshare.13496997>.

Received: 20 May 2020; Accepted: 7 January 2021;

Published online: 18 February 2021

### References

- Nozik, A. J. Photoelectrochemistry: applications to solar energy conversion. *Ann. Rev. Phys. Chem.* **29**, 189–222 (1978).
- Walter, M. G. et al. Solar water splitting cells. *Chem. Rev.* **110**, 6446–6473 (2010).
- Grätzel, M. Photoelectrochemical cells. *Nature* **414**, 338–344 (2001).
- Sivula, K. & Van De Krol, R. Semiconducting materials for photoelectrochemical energy conversion. *Nat. Mater.* **1**, 15010 (2016).
- Montoya, J. H. et al. Materials for solar fuels and chemicals. *Nat. Mater.* **16**, 70–81 (2017).
- Smith, W. A., Sharp, I. D., Strandwitz, N. C. & Bisquert, J. Interfacial band-edge energetics for solar fuels production. *Energy Environ. Sci.* **8**, 2851–2862 (2015).
- Kim, T. W. & Choi, K.-S. Nanoporous BiVO<sub>4</sub> photoanodes with dual-layer oxygen evolution catalysts for solar water splitting. *Science* **343**, 990–994 (2014).
- Pham, T. A., Ping, Y. & Galli, G. Modelling heterogeneous interfaces for solar water splitting. *Nat. Mater.* **16**, 401–408 (2017).
- Nellist, M. R. et al. Potential-sensing electrochemical atomic force microscopy for in operando analysis of water-splitting catalysts and interfaces. *Nat. Energy* **3**, 46–52 (2018).
- Li, D. et al. Crystallographic-orientation-dependent charge separation of BiVO<sub>4</sub> for solar water oxidation. *ACS Energy Lett.* **4**, 825–831 (2019).
- Hu, J., Chen, W., Zhao, X., Su, H. & Chen, Z. Anisotropic electronic characteristics, adsorption, and stability of low-index BiVO<sub>4</sub> surfaces for photoelectrochemical applications. *ACS Appl. Mater. Interfaces* **10**, 5475–5484 (2018).
- Park, Y., McDonald, K. J. & Choi, K.-S. Progress in bismuth vanadate photoanodes for use in solar water oxidation. *Chem. Soc. Rev.* **42**, 2321–2337 (2013).
- Lee, D. K. & Choi, K.-S. Enhancing long-term photostability of BiVO<sub>4</sub> photoanodes for solar water splitting by tuning electrolyte composition. *Nat. Energy* **3**, 53–60 (2018).
- Kuang, Y. et al. Ultrastable low-bias water splitting photoanodes via photocorrosion inhibition and in situ catalyst regeneration. *Nat. Energy* **2**, 16191 (2017).
- Kim, J. H. et al. Hetero-type dual photoanodes for unbiased solar water splitting with extended light harvesting. *Nat. Commun.* **7**, 13380 (2016).
- Zhang, W. et al. Anomalous conductivity tailored by domain-boundary transport in crystalline bismuth vanadate photoanodes. *Chem. Mater.* **30**, 1677–1685 (2018).
- Brongersma, H. H., Draxler, M., de Ridder, M. & Bauer, P. Surface composition analysis by low-energy ion scattering. *Surf. Sci. Rep.* **62**, 63–109 (2007).
- Cushman, C. V. et al. Low energy ion scattering (LEIS). A practical introduction to its theory, instrumentation, and applications. *Anal. Methods* **8**, 3419–3439 (2016).
- Purbaix, M. *Atlas of Electrochemical Equilibria in Aqueous Solutions* (National Association of Corrosion Engineers, 1974).
- Wang, W. et al. The role of surface oxygen vacancies in BiVO<sub>4</sub>. *Chem. Mater.* **32**, 2899–2909 (2020).
- Favaro, M. et al. Chemical, structural, and electronic characterization of the (010) surface of single crystalline bismuth vanadate. *J. Phys. Chem. C.* **123**, 8347–8359 (2019).
- Seo, H., Ping, Y. & Galli, G. Role of point defects in enhancing the conductivity of BiVO<sub>4</sub>. *Chem. Mater.* **30**, 7793–7802 (2018).
- Bjaalie, L., Himmetoglu, B., Weston, L., Janotti, A. & Van De Walle, C. G. Oxide interfaces for novel electronic applications. *N. J. Phys.* **16**, 025005 (2014).
- Balderschi, A., Baroni, S. & Resta, R. Band offsets in lattice-matched heterojunctions: a model and first-principles calculations for GaAs/AlAs. *Phys. Rev. Lett.* **61**, 734–737 (1988).
- Kweon, K. E., Hwang, G. S., Kim, J., Kim, S. & Kim, S. Electron small polarons and their transport in bismuth vanadate: a first principles study. *Phys. Chem. Chem. Phys.* **17**, 256–260 (2015).
- Wiktor, J., Ambrosio, F. & Pasquarello, A. Role of polarons in water splitting: the case of BiVO<sub>4</sub>. *ACS Energy Lett.* **3**, 1693–1697 (2018).
- Wiktor, J. & Pasquarello, A. Electron and Hole Polarons at the BiVO<sub>4</sub>–water interface. *ACS Appl. Mater. Interfaces* **11**, 18423–18426 (2019).
- Reber, J. F. & Meier, K. Photochemical production of hydrogen with zinc sulfide suspensions. *J. Phys. Chem.* **88**, 5903–5913 (1984).
- Govindaraju, G. V., Wheeler, G. P., Lee, D. & Choi, K.-S. Methods for electrochemical synthesis and photoelectrochemical characterization for photoelectrodes. *Chem. Mater.* **29**, 355–370 (2017).
- Nečas, D. & Klapetek, P. Gwyddion: an open-source software for SPM data analysis. *Cent. Eur. J. Phys.* **10**, 181–188 (2012).
- Swartzfager, D. G. Sensitivity factors for surface analysis by ion scattering spectroscopy. *Anal. Chem.* **56**, 55–58 (1984).
- Smith, D. P. Scattering of low-energy noble gas ions from metal surfaces. *J. Appl. Phys.* **38**, 340–347 (1967).
- Perdew, J. P., Burke, K. & Ernzerhof, M. Generalized gradient approximation made simple. *Phys. Rev. Lett.* **77**, 3865–3868 (1996).
- Giannozzi, P. et al. Advanced capabilities for materials modelling with QUANTUM ESPRESSO. *J. Phys. Condens. Matter* **29**, 465901 (2017).
- Giannozzi, P. et al. QUANTUM ESPRESSO: a modular and open-source software project for quantum simulations of materials. *J. Phys. Condens. Matter* **21**, 395502 (2009).
- Hamann, D. R. Optimized norm-conserving Vanderbilt pseudopotentials. *Phys. Rev. B* **88**, 085117 (2013).
- Schlupf, M. & Gygi, F. Optimization algorithm for the generation of ONCV pseudopotentials. *Comput. Phys. Commun.* **196**, 36–44 (2015).
- Cococcioni, M. & De Gironcoli, S. Linear response approach to the calculation of the effective interaction parameters in the LDA+U method. *Phys. Rev. B* **71**, 035105 (2005).
- Sun, W. & Ceder, G. Efficient creation and convergence of surface slabs. *Surf. Sci.* **617**, 53–59 (2013).
- Ong, S. P. et al. Python materials genomics (pymatgen): a robust, open-source python library for materials analysis. *Comput. Mater. Sci.* **68**, 314–319 (2013).
- Hjorth Larsen, A. et al. The atomic simulation environment—a Python library for working with atoms. *J. Phys. Condens. Matter* **29**, 273002 (2017).
- Tersoff, J. & Hamann, D. R. Theory of the scanning tunneling microscope. *Phys. Rev. B* **31**, 805–813 (1985).
- Zhao, Z., Li, Z. & Zou, Z. Structure and energetics of low-index stoichiometric monoclinic clinobisvanite BiVO<sub>4</sub> surfaces. *RSC Adv.* **1**, 874–883 (2011).
- Govoni, M. et al. Qresp, a tool for curating, discovering, and exploring reproducible scientific papers. *Sci. Data* **6**, 190002 (2019).

### Acknowledgements

This work was supported by the National Science Foundation (NSF) under grant no. CHE-1764399. This research used resources of the Center for Functional Nanomaterials, which is a US DOE Office of Science Facility, at Brookhaven National Laboratory under contract no. DE-SC0012704. This research also used computational resources of the University of Chicago's Research Computing Center. This research additionally used resources of the National Energy Research Scientific Computing Center (NERSC), a US Department of Energy Office of Science User Facility located at Lawrence Berkeley National Laboratory, operated under Contract no. DE-AC02-05CH11231. The authors would like to thank R. Farber for helpful discussions in processing STM images.

### Author contributions

K.-S.C., G.G. and M.L. supervised the combined experimental and computational investigations. C.Z. prepared epitaxial BiVO<sub>4</sub> and performed STM imaging and LEIS analysis of BiVO<sub>4</sub>, together with X.T. under the supervision of M.L. D.L. performed all other experimental studies of BiVO<sub>4</sub> under the supervision of K.-S.C. W.W. performed all computational calculations under the supervision of G.G. All authors discussed the results and contributed to writing the manuscript.

### Competing interests

The authors declare no competing interests.

### Additional information

**Supplementary information** The online version contains supplementary material available at <https://doi.org/10.1038/s41560-021-00777-x>.

**Correspondence and requests for materials** should be addressed to M.L., G.G. or K.-S.C.

**Peer review information** *Nature Energy* thanks Fatwa Abdi, Ian Sharp and the other, anonymous, reviewer(s) for their contribution to the peer review of this work.

**Reprints and permissions information** is available at [www.nature.com/reprints](http://www.nature.com/reprints).

**Publisher's note** Springer Nature remains neutral with regard to jurisdictional claims in published maps and institutional affiliations.

© The Author(s), under exclusive licence to Springer Nature Limited 2021